Semi-analytical model for Schottky-barrier carbon nanotube and graphene nanoribbon transistors

Xuebei Yang[†], Gianluca Fiori[‡], Giuseppe Iannaccone[‡], and Kartik Mohanram[†]
[†]Department of Electrical and Computer Engineering, Rice University, Houston
[‡]Information Engineering Department, University of Pisa, Pisa
[†]{xbyang,kmram}@rice.edu [‡]{gfiori,g.iannaccone}@iet.unipi.it

Abstract

This paper describes a physics-based semi-analytical model for Schottky-barrier carbon nanotube (CNT) and graphene nanoribbon (GNR) transistors. The model includes the treatment of (i) both tunneling and thermionic currents, (ii) ambipolar conduction, i.e., both electron and hole current components, (iii) ballistic transport, and (iv) multi-band propagation. Further, it reduces the computational complexity in the two critical and time-consuming steps, namely the calculation of the tunneling probability and the self-consistent evaluation of the the surface potential in the channel. When validated against ViDES, a quantum transport simulation framework based on the non-equilibrium Green's function method, it is several orders of magnitude faster without significant loss in accuracy. Since the model is physics-based, it is parameterizable and can be used to study the effect of common parametric variations in CNT diameter and GNR width, Schottky-barrier height, and insulator thickness.

Categories and Subject Descriptors: B.7.1 [Integrated circuits]: Types and Design Styles—Advanced technologies
General Terms: Design, Performance
Keywords: Carbon nanotubes, graphene nanoribbons, Schottky-barrier, models

1. Introduction

Carbon-based materials such as carbon nanotubes (CNTs) and, more recently, graphene nanoribbons (GNRs), have attracted strong interest as alternative device technologies for future nanoelectronics applications [1–4]. Devices based on these materials offer high mobility for ballistic transport, low drain-induced barrier lowering, high mechanical and thermal stability, and high resistance to electromigration. Although different families of CNTFETs and GNRFETs have been fabricated and studied, the most important distinction is between Schottky-barrier-type (SB-type) and MOSFET-type FETs [5–7]. SB-type FETs (SBFETs henceforth) are the most easily fabricated devices, since they use intrinsic CNT/GNR channels with metallic drain and source contacts. MOSFET-type devices are characterized by doped CNT/GNR channels and Ohmic contacts, and pose more engineering challenges. In SBFETs, a SB is formed between the channel and source/drain contacts and the gate modulates the quantum tunneling current through the SB [5]. It is the tunneling current, as opposed to the thermionic current in MOSFET-type devices, that dominates the device transport. SBFETs are ambipolar, i.e., they conduct both electrons and holes, showing a superposition of n- and p-type behaviors.

Modeling approaches for such novel devices take the form of [8]: (i) computationally intensive, quantum theory based non-equilibrium Green's function (NEGF) approaches [9, 10] or (ii) simpler semi-classical approaches [11–18]. NEGF-based approaches are highly accurate but extremely time consuming. Further, they provide limited intuition necessary for circuit design and optimization with multiple transistors. In comparison to NEGF-based approaches, the simpler semi-classical approaches are computationally very efficient. Further, they are physics-based and parameterizable, providing good intuition to designers. It has been shown that for MOSFET-type transistors, a semi-classical description is valid for a channel length down to about 10nm [12–14, 19].

However, when GNRFETs and CNTFETs are SBFETs where switching behavior stems from the gate modulation of the tunneling probability through the source/drain-channel contacts, a quantum-mechanical description is indispensable [5]. State-of-the-art models for SBFETs, such as [15–18], are based on the semi-classical approach augmented with quantum theory to handle tunneling in SBFETs. The earliest model described in [15] was more efficient than NEGF-based approaches, but still infeasible for routine simulations required for circuit design due to two computationally intensive steps: (i) the calculation of tunneling probability at the SBs and (ii) the self-consistent evaluation of the surface potential in the channel. In [16], the tunneling probability and the surface potential are obtained using approximate closed-form expressions at the cost of physical intuition. In [17, 18], the models are made computationally efficient by considering SBFETs in only the quantum capacitance limit to eliminate the need for self-consistent solution. However, this restricts the use of the model to ultimately scaled devices free of parasitics.

This paper describes an accurate and computationally efficient physics-based semi-analytical model for SB-type CNTFETs and GNRFETs. The model includes the treatment of (i) both tunneling and thermionic currents, (ii) ambipolar conduction, i.e., both electron and hole current components, (iii) ballistic transport, and (iv) multi-band propagation. Further, it reduces the computational complexity in the two critical and time-consuming steps of the semi-classical SBFET modeling approach. First, in the calculation of the tunneling probability through the SB using the Wentzel-Kramers-Brillouin (WKB) approach, we propose linear solutions to substitute for the computationally intensive integral for tunneling probability. Second, in the self-consistent loop to evaluate the surface potential in the channel, we simplify the process to calculate the carrier densities by identifying multiple regions with closed-form solutions. Since the proposed model is physics-based and does not rely on fitting parameters, it can be used to study

This research was supported by NSF grant CCF-0916636.

GLSVLSI'10, May 16–18, 2010, Providence, Rhode Island, USA.

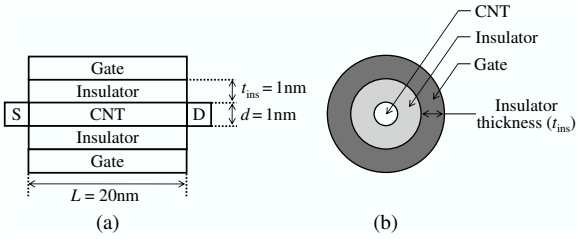

Figure 1: Coaxial CNTFET. (a) and (b) are cross sections along and perpendicular to the channel direction of the CNTFET.

variations in device parameters including CNT diameter and GNR width, insulator thickness, and SB height. When compared to the original semi-classical SBFET model and an NEGF-based quantum transport simulation framework ViDES [10], the proposed model is faster by one and four orders of magnitude, respectively, without significant loss in accuracy.

The paper is organized as follows. We introduce semi-classical SBFET modeling in section 2. In section 3, we describe our approach to reduce the computational complexity of semi-classical SBFET modeling. Section IV presents simulation results and section V is a conclusion.

2. SBFET modeling

Although we consider a coaxial gate geometry SB-type CNTFET with the structure shown in Figure 1 to describe SBFET modeling, the proposed approach can treat other geometries and channel materials, as illustrated for the double-gated GNRFET in Sec. 4.2. The current through the SBFET is calculated using the widely-used Landauer formula [20] and is given by the following expressions:

$$I_{\text{electron}} = \frac{2q}{h}\int_{-\infty}^{\infty}\left(f(E-E_{\text{FS}}) - f(E-E_{\text{FD}})\right)T_{\text{e}}(E)\,\mathrm{d}E$$

$$I_{\text{hole}} = \frac{2q}{h}\int_{-\infty}^{\infty}\left(f(E_{\text{FD}}-E) - f(E_{\text{FS}}-E)\right)T_{\text{h}}(E)\,\mathrm{d}E$$

$$I = I_{\text{electron}} + I_{\text{hole}}$$

where $f()$ is the Fermi function, E_{FS} and E_{FD} are the Fermi levels at the source and the drain, respectively, and T_{e} (T_{h}) is the transmission coefficient for electrons (holes). When all terminal biases are added, the only parameters that remain unknown are the transmission coefficients at the contacts.

Calculating the transmission coefficients: At each contact the transmission coefficients for electron current and hole current need to be calculated, for a total of four coefficients: T_{Se}, T_{Sh}, T_{De} and T_{Dh}. The final transmission coefficients for electrons T_{e} and holes T_{h} are obtained by combining T_{Se}, T_{De} and T_{Sh}, T_{Dh}.

The current is divided into two components: thermionic current,

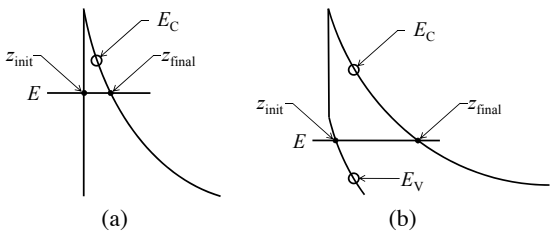

Figure 2: Illustration of the classical turning points. Note that in (b) there is band-to-band tunneling.

which flows above the SBs and tunneling current, which flows through the SB. Whereas the transmission coefficient is 1 for the thermionic current, it is given by the tunneling probability for the tunneling current. The tunneling probability is calculated using the simple but accurate Wentzel-Kramers-Brillouin (WKB) approach that has been widely used in literature [21]. Based on the WKB approach, the tunneling probability T is given by

$$T = \exp\left(-2\int_{z_{\text{init}}}^{z_{\text{final}}} k_{\text{z}}(z)\,\mathrm{d}z\right) \tag{1}$$

where z_{init} and z_{final} are the classical turning points, illustrated in Figure 2, and k_{z} is the parallel momentum related to the E-k relationship of CNTs. Consider electron tunneling for example. k_{z} is given by the expression:

$$k_{\text{z}} = \sqrt{k_n^2 - \left(\frac{E_{\text{g}}/2 - (E_{\text{C}}(z) - E)}{1.5a_{\text{c-c}}V_{\text{pp}\pi}}\right)^2}$$

$$k_n = \frac{|3n-4|}{3R}$$

where k_n is the perpendicular momentum of the nth sub-band, E_{g} is the energy band-gap, $E_{\text{C}}(z)$ is the bottom of the conduction band in the z direction, R is the radius of the CNT, $a_{\text{c-c}}$ is the carbon-carbon bond distance [22], and $V_{\text{pp}\pi}$ is the carbon-carbon bonding energy [23]. Neglecting phase coherence, the overall transmission coefficient is given by [20]:

$$T_{\text{e(h)}} = \frac{T_{\text{Se(Sh)}}T_{\text{De(Dh)}}}{T_{\text{Se(Sh)}} + T_{\text{De(Dh)}} - T_{\text{Se(Sh)}}T_{\text{De(Dh)}}}$$

Modeling the energy band diagram: In order to evaluate the transmission coefficients for the electron and hole tunneling current, the energy profile for the bottom of conduction band $E_{\text{C}}(z)$ and the top of valence band $E_{\text{V}}(z)$ need to be modeled, respectively, as illustrated in Figure 3. For a long channel, where the SBs at the source and drain contacts do not influence each other, the bottom of the conduction band inside the channel E_{bot} is given by the expression:

$$E_{\text{bot}} = \varphi_{\text{SB}} + U_{\text{scf}} + qV_{\text{fb}}$$

where φ_{SB} is the SB height, U_{scf} is the surface potential, and V_{fb} is the flat band voltage. For the coaxial gate geometry, the conduction band E_{C} near the two contacts can be modeled as [17]:

$$E_{\text{C,left}}(z) = \varphi_{\text{SB}} - (\varphi_{\text{SB}} - E_{\text{bot}})(1 - e^{\frac{-2z}{t_{\text{ins}}}})$$

$$E_{\text{C,right}}(z) = (\varphi_{\text{SB}} - qV_{\text{DS}}) - (\varphi_{\text{SB}} - E_{\text{bot}} - qV_{\text{DS}})(1 - e^{\frac{-2(z-L)}{t_{\text{ins}}}})$$

where t_{ins} is the thickness of insulator and L is the channel length. Similarly, the top of the valence band is shifted down by a value of E_{g}, which is the energy gap of the CNT.

Determining the surface potential: The surface potential U_{scf} still remains to be evaluated in order to model the energy band diagram. It is solved through a self- consistent loop [12,14,15] according to:

$$U_{\text{scf}} = U_{\text{L}} + U_{\text{P}}$$

where U_{L} is the Laplace potential due to the applied terminal biases and U_{P} is the potential due to the change in carrier densities. If the substrate is sufficiently thick, $U_{\text{L}} = -qV_{\text{G}}$. Evaluating U_{P} is computationally demanding, however, since it depends on the change in carrier densities as explained below. Consider electrons for illustration. When the terminal biases are zero, the electron density

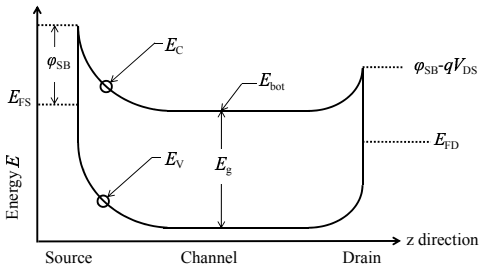

Figure 3: Spatial energy band diagram along the transport direction. E_{FS} and E_{FD} are source and drain Fermi levels.

in the channel is:

$$N_0 = \int_{E_{bot}}^{\infty} D(E) f(E - E_F)\, dE$$

where $D(E)$ is the density of states at the bottom of the conduction band [20] and $f(E - E_F)$ is the Fermi function. Note the integral is from the bottom of the conduction band to infinity. When the terminal biases are not zero, the device is not at equilibrium and the states at the bottom of the conduction band are filled by two different Fermi levels. States with positive velocity (N^+) and negative velocity (N^-) are filled by electrons according to:

$$N^{+(-)} = \frac{1}{2} \int_{E_{bot}}^{\infty} D(E - U_{scf}) f^{+(-)}\, dE$$

Here f^+ and f^- are the Fermi functions modulated by the SBs [15]. U_P is then evaluated as:

$$U_P = \frac{q^2}{C_{ins}} \Delta N = \frac{q^2}{C_{ins}} (N^+ + N^- - N_0)$$

where C_{ins} is the insulator capacitance. Since this U_P is the potential due to the density change in electrons, the effects of holes must be added to obtain:

$$U_P = \frac{q^2}{C_{ins}} (\Delta N_e - \Delta N_h)$$

The most computationally intensive steps of SBFET modeling is thus the self-consistent solution for the surface potential U_{scf}, which has to be repeated for each combination of terminal biases. Within the self-consistent loop, the core computational steps are (i) the evaluation of carrier densities, including electron density and hole density, and (ii) the transmission coefficients T_S and T_D at the source and drain contacts for both electrons and holes. The next section describes the key contributions of this paper to reduce the computational complexity of these steps in SBFET modeling.

3. Reducing computational complexity

In this section, we describe two key simplifications to greatly reduce the computational complexity in SBFET modeling. These simplifications do not rely on fitting parameters, and hence preserve the physics-based properties of the semi-classical approach necessary for parameterized circuit design and optimization.

3.1 The transmission coefficients

While evaluating the transmission coefficient for tunneling current, the integral of k_z in the WKB approach (Equation 1) has to be solved numerically. Traditionally, k_z is calculated at each grid point in the channel between the two turning points and is computationally expensive. In this paper, we derive linear solutions to replace

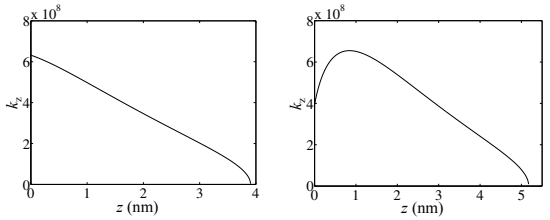

Figure 4: $k_z(z)$ when (a) $E_C(z_{init}) - E < E_g/2$ and (b) $E_C(z_{init}) - E > E_g/2$

this integral as follows. Without loss of generality, consider k_z in the lowest sub-band for the electron tunneling current.

$$\begin{aligned} k_z(z) &= \sqrt{k_n^2 - \left(\frac{E_g/2 - (E_C(z) - E)}{1.5 a_{c\text{-}c} V_{pp\pi}}\right)^2} \\ &= \sqrt{\left(\frac{1}{3R}\right)^2 - \left(\frac{E_g/2 - (E_C(z) - E)}{1.5 a_{c\text{-}c} V_{pp\pi}}\right)^2} \\ &= \frac{1}{1.5 a_{c\text{-}c} V_{pp\pi}} \sqrt{\left(\frac{a_{c\text{-}c} V_{pp\pi}}{2R}\right)^2 - \left(\frac{E_g}{2} - (E_C(z) - E)\right)^2} \\ &= \frac{1}{1.5 a_{c\text{-}c} V_{pp\pi}} \sqrt{\left(\frac{E_g}{2}\right)^2 - \left(\frac{E_g}{2} - (E_C(z) - E)\right)^2} \end{aligned}$$

Note that $E_C(z) - E$ monotonically decreases from z_{init} to z_{final} and $E_C(z_{final}) = E$. Considering the following two cases:

(i) $E_C(z_{init}) - E < E_g/2$: As shown in Figure 4(a), $k_z(z)$ decreases monotonically. The integral in Equation 1 is the area between the x-axis, y-axis, and $k_z(z)$, which is roughly the area of a triangle. Hence, the integral can be simplified to the product of $k_z(\frac{z_{init} + z_{final}}{2})$ and $z_{final} - z_{init}$.

(ii) $E_C(z_{init}) - E > E_g/2$: As shown in Figure 4(b), $k_z(z)$ increases first, then decreases monotonically. The integral in Equation 1, or the area between the x-axis, y-axis, and $k_z(z)$, can be regarded as the area of a triangle and a trapezoid. The triangle and the trapezoid are separated at z_{peak}, where z_{peak} satisfies $E_C(z_{peak}) - E = E_g/2$ and $k_z(z_{peak})$ reaches its maximum. From the model for the energy band diagram,

$$z_{peak} = \frac{t_{ins}}{2} \ln \frac{\varphi_{SB} - E_{bot}}{E + E_g/2 - E_{bot}}$$

Hence, the integral can be simplified to

$$\frac{k_z(z_{peak})}{2}(z_{final} - z_{peak}) + \frac{(k_z(z_{init}) + k_z(z_{peak}))}{2}(z_{peak} - z_{init})$$

Therefore, instead of computing k_z at each grid point in the channel between the two turning points, the transmission coefficients can be evaluated using only one or two expressions for k_z. This reduces the computation time significantly, with negligible impact on accuracy, as presented in Sec. 4.

3.2 Electron and hole densities

In the self-consistent loop, the calculation of U_P is computationally demanding since the change in both electron density and hole density must be evaluated numerically at each grid point. In our work, we propose a transformation that simplifies the calculation of carrier densities as follows. Without loss of generality, consider electron density. The density of electrons in positive velocity states N^+ and in negative velocity states N^- are:

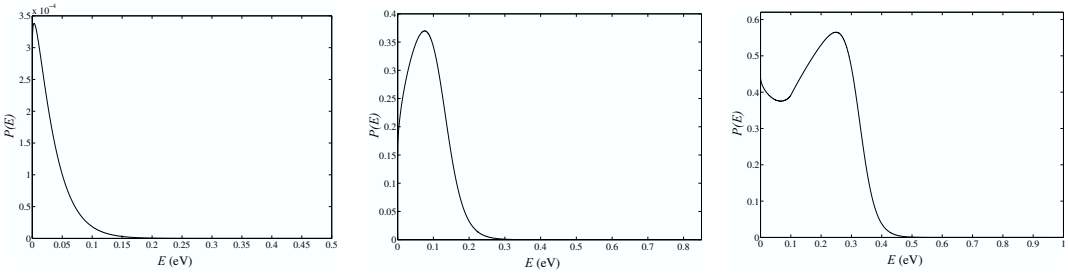

(a) (b) (c)

Figure 5: (a) $E_{\text{bot}} > E_{\text{exp}}$, (b) $E_{\text{bot}} < E_{\text{exp}}$ and $\varphi_{\text{SB}} - E_{\text{bot}} < V_{\text{DS}}$, (c) $E_{\text{bot}} < E_{\text{exp}}$, $\varphi_{\text{SB}} - E_{\text{bot}} > V_{\text{DS}}$ and $\varphi_{\text{SB}} - V_{\text{DS}} < E_{\text{exp}}$

$$
\begin{aligned}
N^+ &= \frac{1}{2}\int_{E_{\text{bot}}}^{\infty} D(E-U_{\text{scf}})f^+ \,\mathrm{d}E \\
&= \frac{1}{2}\int_{E_{\text{bot}}}^{\infty} D(E-U_{\text{scf}})\frac{T_{\text{S}}f_{\text{S}}+T_{\text{D}}f_{\text{D}}-T_{\text{S}}T_{\text{D}}f_{\text{D}}}{T_{\text{S}}+T_{\text{D}}-T_{\text{S}}T_{\text{D}}}\,\mathrm{d}E \\
&= \int_{E_{\text{bot}}}^{\infty} \frac{D_0(E-E_{\text{bot}}+E_{\text{g}}/2)(T_{\text{S}}f_{\text{S}}+T_{\text{D}}f_{\text{D}}-T_{\text{S}}T_{\text{D}}f_{\text{D}})}{2\sqrt{(E-E_{\text{bot}}+E_{\text{g}}/2)^2-(E_{\text{g}}/2)^2}(T_{\text{S}}+T_{\text{D}}-T_{\text{S}}T_{\text{D}})}\,\mathrm{d}E
\end{aligned}
$$

Similarly,

$$
N^- = \int_{E_{\text{bot}}}^{\infty} \frac{D_0(E-E_{\text{bot}}+E_{\text{g}}/2)(T_{\text{S}}f_{\text{S}}+T_{\text{D}}f_{\text{D}}-T_{\text{S}}T_{\text{D}}f_{\text{S}})}{2\sqrt{(E-E_{\text{bot}}+E_{\text{g}}/2)^2-(E_{\text{g}}/2)^2}(T_{\text{S}}+T_{\text{D}}-T_{\text{S}}T_{\text{D}})}\,\mathrm{d}E
$$

Here, f_{S} and f_{D} are Fermi function of the source and the drain respectively. The total electron density is equal to $N^+ + N^-$. Since both f_{S} and f_{D} that include exponential terms appear in both N^+ and N^-, we rearrange terms to simplify the integrals as follows.

$$
\begin{aligned}
N_1 &= \frac{D_0}{2}\int_{E_{\text{bot}}}^{\infty} \frac{E-E_{\text{bot}}+E_{\text{g}}/2}{\sqrt{(E-E_{\text{bot}}+E_{\text{g}}/2)^2-(E_{\text{g}}/2)^2}}\frac{2T_{\text{S}}f_{\text{S}}-T_{\text{S}}T_{\text{D}}f_{\text{S}}}{T_{\text{S}}+T_{\text{D}}-T_{\text{S}}T_{\text{D}}}\,\mathrm{d}E \\
N_2 &= \frac{D_0}{2}\int_{E_{\text{bot}}}^{\infty} \frac{E-E_{\text{bot}}+E_{\text{g}}/2}{\sqrt{(E-E_{\text{bot}}+E_{\text{g}}/2)^2-(E_{\text{g}}/2)^2}}\frac{2T_{\text{D}}f_{\text{D}}-T_{\text{S}}T_{\text{D}}f_{\text{D}}}{T_{\text{S}}+T_{\text{D}}-T_{\text{S}}T_{\text{D}}}\,\mathrm{d}E
\end{aligned}
$$

Note that since $N^+ + N^-$ is equal to $N_1 + N_2$, rearranging terms does not change the final result. By making the substitution

$$
E' = \sqrt{(E-E_{\text{bot}}+E_{\text{g}}/2)^2-(E_{\text{g}}/2)^2}
$$

and setting

$$
E = \sqrt{(E')^2+(E_{\text{g}}/2)^2} - E_{\text{g}}/2 + E_{\text{bot}},
$$

N_1 and N_2 can be written as:

$$
N_1 = \frac{D_0}{2}\int_0^{\infty} \frac{2T_{\text{S}}(E)-T_{\text{S}}(E)T_{\text{D}}(E)}{T_{\text{S}}(E)+T_{\text{D}}(E)-T_{\text{S}}(E)T_{\text{D}}(E)}f_{\text{S}}(E)\,\mathrm{d}E'
$$

$$
N_2 = \frac{D_0}{2}\int_0^{\infty} \frac{2T_{\text{D}}(E)-T_{\text{S}}(E)T_{\text{D}}(E)}{T_{\text{S}}(E)+T_{\text{D}}(E)-T_{\text{S}}(E)T_{\text{D}}(E)}f_{\text{D}}(E)\,\mathrm{d}E'
$$

The integrals are then simplified as follows, and we illustrate this by considering N_1:

$$
\begin{aligned}
N_1 &= \frac{D_0}{2}\int_0^{\infty} \frac{2T_{\text{S}}(E)-T_{\text{S}}(E)T_{\text{D}}(E)}{T_{\text{S}}(E)+T_{\text{D}}(E)-T_{\text{S}}(E)T_{\text{D}}(E)}f_{\text{S}}(E)\,\mathrm{d}E' \\
&= \frac{D_0}{2}\int_0^{\infty} T(E)f_{\text{S}}(E)\,\mathrm{d}E' \\
&= \frac{D_0}{2}\int_0^{\infty} P\left(\sqrt{(E')^2+(E_{\text{g}}/2)^2}-E_{\text{g}}/2+E_{\text{bot}}\right)\mathrm{d}E' \\
&= \frac{D_0}{2}\int_0^{\infty} P(E')\,\mathrm{d}E' \qquad (2)
\end{aligned}
$$

In order to simplify the integral, it is necessary to investigate the shape of $P(E')$. $P(E')$ is the product of two terms: the Fermi function and the transmission coefficient (T-term). At low energies, the Fermi function is always close to 1 and the T-term dominates the shape of $P(E')$. When the energy increases, the Fermi function has an exponential behavior, and changes in the value of the T-term are slow in comparison to the exponential fall-off in the value of the Fermi function. Hence, the shape of $P(E')$ is dominated by the Fermi function in this regime. We assume that Fermi function begins to exhibit exponential behavior at the energy $E' = E_{\text{exp}}$ where $f_{\text{S}}(\sqrt{E_{\text{exp}}^2+(E_{\text{g}}/2)^2} - E_{\text{g}}/2 + E_{\text{bot}}) \approx 0.90$. With this boundary condition, we divide the problem into the following regimes, as illustrated in Figure 5:

1. $E_{\text{bot}} > E_{\text{exp}}$

   $P(E')$ is monotonically decreasing in this situation. In order to simplify the integral, we use the bisection method to find the point $E' = E_{\text{m}}$ where $P(E_{\text{m}}) = 1/2P(0)$, and approximate the integral in Equation 2 to $2P(E_{\text{m}})\cdot E_{\text{m}}$.

2. $E_{\text{bot}} < E_{\text{exp}}$ and $\varphi_{\text{SB}} - E_{\text{bot}} < V_{\text{DS}}$

   Under these conditions, there are two regions separated by E_{exp}. In the first region, the Fermi function is almost constant and the T-term dominates the shape of the curve. Upon closer examination, it is clear that the T-term is equal to $T_{\text{S}}(E)$ because $T_{\text{D}}(E) = 1$. We use a linear function to simplify the integral by calculating $T_{\text{S}}(E_{\text{exp}}/2)$, and simplify the integral in this region to $T_{\text{S}}(E_{\text{exp}}/2)\cdot E_{\text{exp}}$. In the second region, the Fermi function dominates, and the conditions are similar to $E_{\text{bot}} > E_{\text{exp}}$ above. The total value of the integral in Equation 2 is given by the sum of the two regions.

3. $E_{\text{bot}} < E_{\text{exp}}$ and $\varphi_{\text{SB}} - E_{\text{bot}} > V_{\text{DS}}$

   Under these conditions, there may be two or three regions, depending on whether $\varphi_{\text{SB}} - V_{\text{DS}}$ is above E_{exp} or not. If $\varphi_{\text{SB}} - V_{\text{DS}} \geq E_{\text{exp}}$, it is similar to condition (2) above. There are two regions, with the T-term dominating the first. Although the T-term is not equal to $T_{\text{S}}(E)$, it is still possible to use a linear function to simplify the integral. In the second region, the Fermi function dominates and it is equivalent to case (1) above. If $\varphi_{\text{SB}} - V_{\text{DS}} < E_{\text{exp}}$, there are three regions. The first interval is from from 0 to the point where $\sqrt{(E')^2+(E_{\text{g}}/2)^2} - E_{\text{g}}/2 + E_{\text{bot}} = \varphi_{\text{SB}} - V_{\text{DS}}$. If the energy increases to E_{exp}, it is in the second region where only the source has SBs. In both regions, we use a linear function to simplify the integral. Finally, the third region uses the same conditions as (1) above.

Although the self-consistent loop is still needed to evaluate U_{scf}, simplifying the calculation of the transmission coefficients and the carrier densities reduces the computational burden in the two core

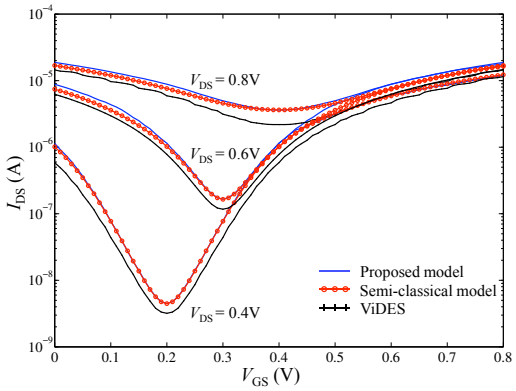

Figure 6: Model validation for $V_{DS} = 0.4$V, 0.6V, and 0.8V.

loops significantly. Hence, the overall complexity of the semi-classical SBFET model is reduced without loss in accuracy.

4. Results and discussions

We begin by comparing the results of our proposed semi-analytical model to the original semi-classical model as well as to the rigorous quantum atomistic simulator ViDES [10]. We consider a CNTFET with coaxial gate geometry and a 20nm long (13,0) CNT channel. The gate insulator is SiO_2 with $t_{ins} = 1$nm. The SB height is assumed to be half of the band-gap. In Figure 6, we compare the I-V curves obtained from our semi-analytical model, the original semi-classical model, and ViDES, respectively, for several bias points. Ambipolar characteristics due to both electron and hole conduction are clearly shown, and the drain voltage exponentially increases the minimum leakage current. The point of minimum current is at $V_{GS} = V_{DS}/2$. As drain voltage increases, SBFETs show linear behavior in the overall range of gate bias. For example, the drain current and the channel charge for $V_{DS} = 0.8$V are linearly proportional to V_{GS}, whereas those for $V_{DS} = 0.4$V show exponential behavior in the sub-threshold region. Note that the difference between the results of the proposed semi-analytical model and the original semi-classical model is very small, which demonstrates that our simplification does not result in significant loss of accuracy. In comparison, the difference between the results of the proposed model and ViDES is slightly higher. This can be attributed to the difference in the calculation of the transmission coefficients between the semi-classical and quantum approaches. ViDES considers phase coherence of scattering at the two SBs and the energy profile is more rigorous, which explains the oscillating nature of the computed transmission coefficient. However, since this treatment is at the atomic level and extremely computationally intensive, it is not feasible in semi-classical approaches. Table 1 presents the average computational time for 80 bias points for ViDES, the original semi-classical model, and the proposed model. Our semi-analytical model is one order of magnitude faster than the original semi-classical model and four orders of magnitude faster than ViDES.

Table 1: Average computational time for ViDES, original semi-classical SBFET model, and the proposed model.

Model	Time
ViDES	8-10 hours
Semi-classical SBFET model	20-30 seconds
Proposed semi-analytical model	2-4 seconds

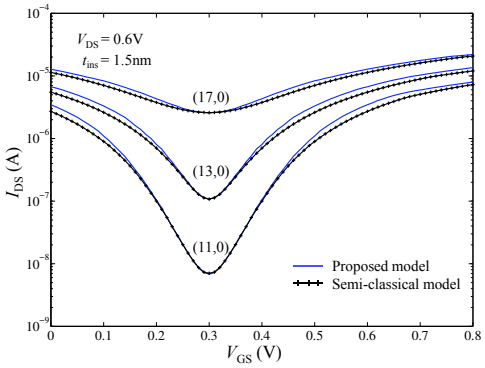

Figure 7: The effect of CNT chirality on the drain current. $V_{DS} = 0.6V$, t_{ins} is 1.5nm, and channel length is 20nm.

4.1 Parameter variations

Parameter variations play an important role in CNTFET electronics because they significantly influence both the "on" and "off" current. Typical parameters considered in CNTFET simulation and design include CNT chirality, insulator thickness, and SB height. Our model is able to simulate the effect of parameter variations. Although prior work [9,15] has investigated these problems in detail using rigorous simulation approaches, our semi-analytical model is able to provide results that are consistent with these more rigorous approaches in a fraction of the time. In this section, we will present the simulation results of variations in CNT chirality (and hence, diameter), insulator thickness, and SB height.

CNT chirality: The diameter of a CNT is determined by the chirality, while the energy band-gap is inversely proportional to the diameter. We simulated (11,0), (13,0), and (17,0) CNTFETs, and the results are shown in Figure 7. As the diameter increases, the band-gap decreases. This allows more electrons and holes in the conduction and valence bands, respectively, thereby increasing the current. However, a small band-gap also increases the "off" current, so the I_{on}/I_{off} ratio is lower.

Insulator thickness: The insulator thickness t_{ins} influences the SB thickness and the gate capacitance. As t_{ins} increases, the SBs at the two channel ends also become thicker and the gate capacitance decreases. A low gate capacitance means the gate has less control over the drain current, and a thick SB lowers the tunneling probability. Therefore, when t_{ins} increases, the current decreases. We simulated a CNTFET with gate insulator thickness at 1nm, 2nm, and 3nm, and the results are shown in Figure 8.

SB height: The most commonly studied devices are mid-gap SBFETs, i.e., $\varphi_{SB} = E_g/2$, and all the simulations so far have only considered mid-gap transistors. Under this condition, the minimum current occurs at $V_{GS} = V_{DS}/2$. However, depending on the contact work functions, the SB height can differ from $E_g/2$ [24]. As the SB height increases, the electron current is lowered and hole current is larger, so that the right branch of the curve is shifted down, the left branch shifted up, and the minimum current point moves to the right. When the SB height decreases, the right branch shifts up, the left branch shifts down, and the minimum current point shifts to the left, as shown in Figure 9. Our results for $\varphi_{SB} = 0$, $E_g/2$, and E_g are shown in Figure 9.

4.2 GNRFET simulation

So far, this paper has only considered CNTFETs. However, our model can also be used to simulate GNRFETs. Since GNRs and CNTs share many properties, only a few changes are needed. The

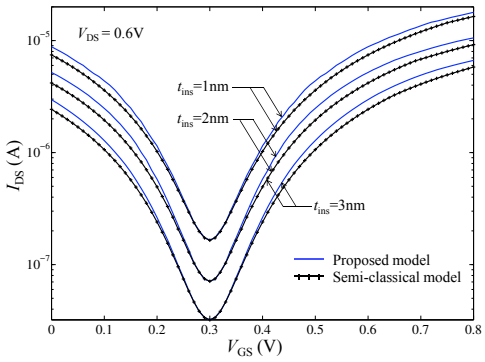

Figure 8: The effect of insulator thickness on the drain current. $V_{DS} = 0.6V$, default gate insulator dielectric constant is 3.9, and channel length is 20nm.

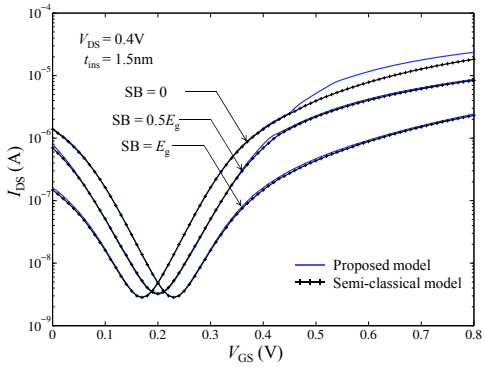

Figure 9: The effect of SB height on the drain current. $V_{DS} = 0.4V$, insulator thickness is 1.5nm and channel length is 20nm.

major changes include: (i) the energy band-gap of a GNR is determined by its width instead of the chiralities, (ii) GNRFETs usually do not have coaxial structures, so the expressions for gate capacitance and energy band diagram need to be changed depending on the structure (double-gate in our case), and (iii) k_z [18] for GNRs has a linear relationship with energy that makes the integral of k_z in the WKB even simpler. By making these changes, our model is compatible with GNRFETs, and the major ideas and simplification approaches mostly remain valid. Figure 10 presents results comparing our model and ViDES for a double-gated GNRFET with an N=12 armchair-edge GNR channel and $t_{ins} = 2$nm. Further, the proposed model can also incorporate the effects of edge bond relaxation and third nearest neighbor interactions that have been shown to play an important role in GNRs.

5. Conclusions

Carbon-based materials are potential candidates for nanoelectronics applications. An important challenge is the development of accurate and computationally efficient models. Although some models have been proposed recently, they are either computationally expensive or unable to give the physical intuition of the devices. This paper described a semi-analytical model suitable for the treatment of Schottky-barrier FETs. The model relies on physics-based methods to reduce the computational complexity by simplifying the calculation of transmission coefficient and the carrier densities. When compared to the full quantum-theory-based simulator ViDES and the original semi-classical model, the proposed model is four orders and one order of magnitude faster, respectively, without significant loss of accuracy.

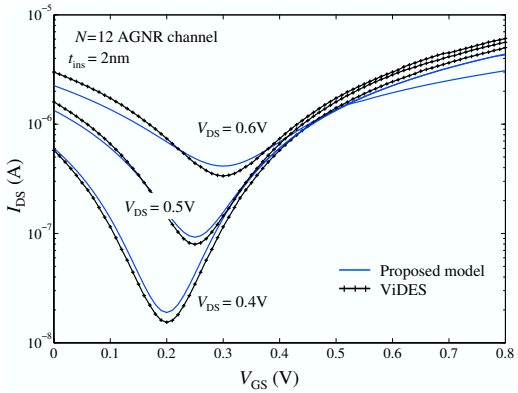

Figure 10: Results for a GNRFET with N=12 armchair-edge GNR channel and t_{ins} = 2nm.

References

[1] P. Avouris *et al.*, "Carbon nanotube electronics," *Proc. IEEE*, vol. 91, pp. 1772–1784, Nov. 2003.

[2] A. Javey *et al.*, "High performance n-type carbon nanotube field-effect transistors with chemically doped contacts," *Nano Letters*, vol. 5, pp. 345–348, 2005.

[3] A. Geim and N. Novoselov, "The rise of graphene," *Nature Materials*, vol. 6, pp. 183–191, 2007.

[4] P. Avouris, Z. Chen, and V. Perebeinos, "Carbon-based electronics," *Nature Nanotechnology*, vol. 2, pp. 605–615, 2007.

[5] S. Heinze *et al.*, "Carbon nanotubes as Schottky barrier transistors," *Phys. Rev. Lett.*, vol. 89, p. 106801, 2002.

[6] A. Javey *et al.*, "Ballistic carbon nanotube field-effect transistors," *Nature*, vol. 424, pp. 654–657, 2003.

[7] X. Li *et al.*, "Chemically derived, ultrasmooth graphene nanoribbon semiconductors," *Science*, vol. 319, pp. 1229–1232, Feb. 2008.

[8] M. P. Anantram, M. S. Lundstrom, and D. E. Nikonov, "Modeling of nanoscale devices," *Proc. IEEE*, vol. 96, pp. 1511–1550, 2008.

[9] J. Guo, S. Datta, and M. Lundstrom, "A numerical study of scaling issues for Schottky-barrier carbon nanotube transistors," *IEEE Trans. on Electron Devices*, vol. 51, pp. 172–177, 2004.

[10] G. Fiori and G. Iannaccone, "NanoTCAD ViDES," 2008. DOI: 10254/nanohub-r5116.3.

[11] T. Nakanishi *et al.*, "Transport through the interface between a semiconducting carbon nanotube and a metal electrode," *Phys. Rev. B*, vol. 66, p. 073307, 2002.

[12] A. Rahman *et al.*, "Theory of ballistic nanotransistors," *IEEE Trans. on Electron Devices*, vol. 50, pp. 1853–1864, Sep. 2003.

[13] K. Natori, Y. Kimura, and T. Shimizu, "Characteristics of a carbon nanotube field-effect transistor analyzed as a ballistic nanowire field-effect transistor," *Jnl. Applied Physics*, vol. 97, p. 343061, Feb. 2005.

[14] J. Deng and H. Wong, "A compact SPICE model for carbon-manotube field-effect transistors including nonidealities and its application — Part I: Model of the intrinsic channel region," *IEEE Trans. on Electron Devices*, vol. 54, pp. 3186–3194, Dec. 2007.

[15] A. Hazeghi, T. Krishnamohan, and H. Wong, "Schottky-barrier carbon nanotube field-effect transistor modeling," *IEEE Trans. on Electron Devices*, vol. 54, pp. 439–445, Mar. 2007.

[16] A. Balijepalli *et al.*, "Compact modeling of carbon nanotube transistor for early stage process-design exploration," in *Proc. Intl. Symposium on Low Power Electronics and Design*, pp. 2–7, Aug. 2007.

[17] D. Jimenez *et al.*, "A simple drain current model for Schottky-barrier carbon nanotube field effect transistors," *Nanotechnology*, vol. 18, p. 025201, Jan. 2007.

[18] D. Jimenez, "A current-voltage model for Schottky-barrier graphene-based transistors," *Nanotechnology*, vol. 19, p. 345204, Aug. 2008.

[19] R. Venugopal *et al.*, "Simulating quantum transport in nanoscale transistors: Real versus mode-space approaches," *Jnl. of Applied Physics*, vol. 92, pp. 3730–3739, 2002.

[20] S. Datta, *Electronic Tansport in Mesoscopic Systems*. Cambridge University Press, 1995.

[21] N. H. Frank and L. A. Young, "Transmission of electrons through potential barriers," *Phys. Rev.*, vol. 38, pp. 80–86, 1931.

[22] P. Avouris, M. Radosavljevic, and S. Wind, *Carbon Nanotube Electronics and Optoelectronics*, pp. 227–251. Springer, 2005.

[23] J. Mintmire and C. White, "Universal density of states for carbon nanotubes," *Phys. Rev. Lett.*, vol. 81, p. 206803, 1998.

[24] J. L. Freeouf and J. M. Woodall, "Schottky barriers: An effective work function model," *Appl. Phys. Lett.*, vol. 39, pp. 727–729, Nov. 1981.